Room-Temperature Fabrication of p-Type SnO Semiconductors by Ion-Beam-Assisted Deposition

Mochamad Januar,[†,△] Suhendro Purbo Prakoso,[‡,△] Chia-Wen Zhong,[¶] Chuan Li,[§] Jang-Hsing Hsieh,[§,‖] Horng-Chih Lin,[¶] Kuo-Kang Liu,[⊥] and Kou-Chen Liu[*,†,#,@]

†*Department of Electronic Engineering, Chang Gung University, Taoyuan 33302, Taiwan*

‡*Department of Chemical Engineering, National Taiwan University of Science and Technology, Taipei City 10607, Taiwan*

¶*Department of Electronics Engineering and Institute of Electronics, National Yang Ming Chiao Tung University, Hsinchu 300, Taiwan.*

§*Department of Biomedical Engineering, National Yang Ming Chiao Tung University, Hsinchu 300, Taiwan.*

‖*Center for Plasma and Thin Film Technologies, Ming Chi University of Technology, New Taipei City 24301, Taiwan.*

⊥*School of Engineering, University of Warwick, Coventry CV4 7AL, United Kingdom.*

#*Division of Pediatric Infectious Disease, Department of Pediatrics, Chang Gung Memorial Hospital, Linkou 33305, Taiwan*

@*Department of Materials Engineering, Ming Chi University of Technology, New Taipei City 24301, Taiwan*

△*These authors contributed equally to this work*

Received June 27, 2022; E-mail: jacobliu@mail.cgu.edu.tw

Abstract: Over the past decade, SnO has been considered a promising p-type oxide semiconductors. However, the achievement of high mobility in the fabrication of p-type SnO films is still highly dependent on the post-annealing procedure, which often makes SnO, due to its metastable nature, easy to convert into SnO_2 and/or intermediate phases. This paper demonstrates the fully room-temperature fabrication of p-type SnO_x thin films using ion-beam-assisted deposition. This technique offers independent control between ion density, *via* the ion-gun anode current and oxygen flow rate, and ion energy, *via* the ion-gun anode voltage, thus being able to significantly optimize the hole mobility and the optical bandgap of SnO to reach 7.89 $cm^2V^{-1}s^{-1}$ and 2.70 eV, respectively, without the need for annealing. Due to the absence of the annealing process, the Raman spectra reveal no significant signatures of microcrystal formation in the films. This contrasts with the case involving the air-annealing procedure, where a complex interaction occurs between the formation of SnO microcrystals and the formation of SnO_x intermediate phases. This interplay results in variations in grain texture within the film, leading to a lower optimum Hall mobility of only 5.17 $cm^2V^{-1}s^{-1}$. Finally, we demonstrate the rectification characteristics of all-fabricated-at-room-temperature SnO_x-based p-n devices to confirm the viability of the p-type SnO_x films.

The development of oxide semiconductors has attracted great interest due to their compatibility with low-temperature processes to support many emerging applications, including transparent and flexible displays and transparent complementary-metal-oxide-semiconductor (CMOS) circuits.[1,2] For instance, transparent amorphous InGaZnO with mobility greater than 10 $cm^2V^{-1}s^{-1}$ has been successfully fabricated at room temperature and has proven useful in driving thin-film transistors in flat panels and flexible displays.[1,3] Unfortunately, p-type oxide semiconductors with mobility comparable to such n-type are difficult to achieve because the valence band (VB) as a hole conduction pathway in these materials inherently consists of highly localized and anisotropic O $2p$ orbitals.[4] It is their poor p-type that hinders the application of oxide semiconductors in low-power and high-performance transparent CMOS logic circuits, where a balanced performance across the p- and n-type devices is essential.[5,6] Recently, several oxide materials have been proposed to produce high-performance transparent p-type semiconductors, including copper-based ternary oxides ($CuMO_2$, M = Al, Ga, In, *etc.*),[7] spinel oxides (ZnM_2O_4, M = Rh, Co, Ir),[8] and tin monoxide (SnO).[9,10] Among these oxides, SnO is the most attractive p-type candidate due to its potential to exhibit equivalently high hole mobility and simultaneously possess a sufficiently transparent optical bandgap (∼2.70 eV).[10–15] The characteristic of hole mobility in SnO stems from the modification of the valence band maxima (VBM) due to the overlapping of the O $2p$ and Sn $5s$ orbitals, so the hole transport path is more delocalized than a typical oxide semiconductor whose VBM consists of only O $2p$ orbitals.[9] Nevertheless, in contrast to the n-type oxides which are readily produced at room temperature, the success of producing high-mobility p-type SnO films so far still relies heavily on the thermal annealing procedures.[12–16] Reports focusing on the development of room-temperature fabrications for p-type SnO thin films are scarce in the literature,[17,18] and thus still represent a major challenge. Yet, this aspect needs to be addressed in order for the p-type oxides to be technologically commensurate with their n-type counterparts.[4]

To date, the feasibility of p-type conductivity in SnO has been experimentally demonstrated using several techniques, including reactive magnetron sputtering,[14,15,19] atomic layer deposition,[5,20] pulsed laser deposition,[10,12,21] e-beam evaporation,[6,22,23] and solution process.[13,24] However, the performance of the prepared SnO still varies greatly depending on the type of sample and the resulting crystal structure. For bulk SnO polycrystals, hole mobility as high as 30.0 $cm^2V^{-1}s^{-1}$ has been reported.[13] In contrast, for thin-film SnO, the reported hole mobility is drastically lower, which is about 2.4 $cm^2V^{-1}s^{-1}$ for epitaxial films[10,21] and less than

5.0 $cm^2V^{-1}s^{-1}$ for polycrystalline films.[25–27] Not to mention the non-annealed nanocrystalline SnO films, whose mobility is even lower[17,27,28] and often unmeasurable[18,29,30] due to their higher structural disorders. Theoretical studies have identified that the source of the *p*-type conductivity of SnO is mainly associated with the Sn vacancy (V_{Sn}^{2-}).[9,31] Since the presence of too much V_{Sn}^{2-} can also act as scattering centers for the hole carriers,[32] precise control of the native defects is required to obtain sufficient hole concentration as well as maintain a lower scattering effect. Hence, it is expected that the hole mobility can be increased by decreasing the carrier density through fine-tuning the defect level in the deposition process. As recently demonstrated by Minohara *et al.*,[12,16] the mobility of the SnO epitaxial film can be boosted up to 21.0 $cm^2V^{-1}s^{-1}$ at a lower hole concentration of 7.0×10^{16} cm^{-3}, which was achieved by modulating laser fluence and growth temperature in pulsed laser deposition. Furthermore, hole mobility up to 18.7 $cm^2V^{-1}s^{-1}$ can also be achieved in polycrystalline SnO films prepared using the more industrially compatible magnetron-sputtering technology.[14,15] Such high mobility was achieved by incorporating a controlled β-Sn metal in the SnO film, leaving the SnO film in a slightly Sn-rich state. The native defects in the Sn-rich state, particularly the Sn interstitials (Sn_i), can enhance the *s*-orbital character in the upper VB state, which makes the VBM more delocalized and the hole mobility further improved.[33,34] However, similar to V_{Sn}^{2-}, excess Sn metals also have the potential to act as charge-carrier scatterers, which might counteract the high mobility.[14,33] Therefore, tuning the SnO native defects in the deposition process is critical to find a balance between the scattering and the mobility enhancement.

The usual strategy for defect tuning is to optimize the thermodynamic conditions based on the defect equilibrium,[12] which is usually accomplished (as noted above) by performing high-temperature annealing either during or after deposition.[10,12–16,21,25–27] However, for SnO, the thermodynamic window is quite narrow due to its thermal instability, which leads to the potential issues concerning the uniformity over a large area.[35] The metastable nature of the SnO phase makes them easy to disproportionate to the more thermodynamically stable SnO_2 phase at high temperatures.[14,36,37] It was reported that the disproportionation started at 300 °C when annealing was carried out in the absence of an oxygen source,[23] and it started at a lower temperature at 180 °C when annealing was carried out in an oxidizing environment.[26] Hence, this approach runs the risk of producing SnO films containing mixed phases of SnO_2 and its intermediate phase.[5,25,38] These coexisting phases generate Sn^{4+} ions and/or associated defect states, which act as hole compensators, at a perceptible rate in some regions of the film, thereby deteriorating the uniformity of its electrical performance.[15,25,35,38] Thus, it would be ideal if *p*-type SnO thin films could be produced without having to go through an annealing process.

Interestingly, a recent theoretical study revealed that the *s*-orbital character of the Sn-rich SnO films is retained even when the film structure is amorphous.[18] In the Sn-rich condition, the excess Sn atoms tend to form stabilizing clusters that consolidate the Sn $5s^2$ lone-pair states, similar to the lone-pair distortion of the layer structure in the crystalline phase.[39] This clustering of lone pairs leads to a VBM with substantial metallic *s*-orbital character, potentially facilitating the formation of a hole conduction pathway even though the SnO film is in an amorphous state.[18,40] This concept opens up great opportunities to develop high mobility SnO thin films using fully room-temperature processes, which are prone to being amorphous or nanocrystalline.[27,41] Therefore, it is necessary to develop alternative thin-film deposition techniques that can facilitate controlled oxidation of SnO (for defect tuning) at room temperature. Deposition at room temperature can be a promising advantage not only for precluding phase decomposition in the *p*-type SnO films, but also for establishing processes on flexible substrates to support the development of flexible electronics.

In this paper, we demonstrate the fully room-temperature fabrication of *p*-type SnO films using ion-beam-assisted deposition (IBAD). Production of Sn-based oxide films using the IBAD technique has been previously reported,[42–44] but none of these studies focused on obtaining the *p*-type conductivity of the oxide films. Thus, to our knowledge, this is the first report demonstrating *p*-type conduction in SnO films using the IBAD technique. Compared to conventional magnetron sputtering, IBAD offers independent control of processing parameters, namely the vapor deposition rate and the ion-flux conditions. The vaporized Sn metal in the IBAD system is controlled by an *e*-beam source, and the ion flux responsible for oxidizing the vapor is generated independently by an ion source (see the illustration in Fig. 1). While the Sn vapor condenses on the substrate at the desired deposition rate to form the thin film, independently controllable highly energetic ions can be directed at the growing thin layer. These energetic ions enable the oxidation of metallic Sn at room temperature through an ion-bombardment process.[43,44] Using this approach, we show here that SnO films with Hall mobility of 7.89 $cm^2V^{-1}s^{-1}$, a hole concentration of 4.9×10^{16} cm^{-3}, and an optical bandgap of 2.70 eV can be achieved without annealing. It is worth noting that this is the highest mobility reported for the *p*-type SnO films whose fabrication was carried out entirely at room temperature (see Table 1). We varied the ion-flux parameters, namely anode current (I_A) and anode voltage (V_A) (see the inset figure), at a fixed deposition rate and examined their impact on electrical and optical performances using Hall-effect and UV-visible measurements, respectively. The microstructural phases of the resulting SnO_x films were studied in detail using Raman spectroscopy. Post-annealing procedures in vacuum and air were also performed for comparison. We found that the room-temperature process is more desirable because the resulting films have a relatively more controllable electrical performance compared to the air-annealed samples. We rationalized the origin of mobility in the annealed and non-annealed SnO_x films based on Urbach's rule, Raman spectroscopy, and theoretical insights from the first-principle calculations. Finally, the feasibility of this material in an electronic device was demonstrated by fabricating transparent *p*-*n* junction diodes consisting of the SnO_x films deposited on ITO substrates. The successful preparation and application of room-temperature *p*-type SnO films by the IBAD technique suggest that they may have a promising future in large-scale industrial applications, particularly for large-area and flexible electronic devices.

Figure 2 shows a process window that can produce *p*-type and *n*-type SnO_x films through variations in the ion-gun anode current and oxygen flow rate (OFR) in the IBAD system. Clear *p*-type conductivity, with the Hall mobility increasing from 0.47 $cm^2V^{-1}s^{-1}$ to 1.18 $cm^2V^{-1}s^{-1}$ (see Fig. 2(a)) and the carrier concentration decreasing from 1.4×10^{19} cm^{-3} to

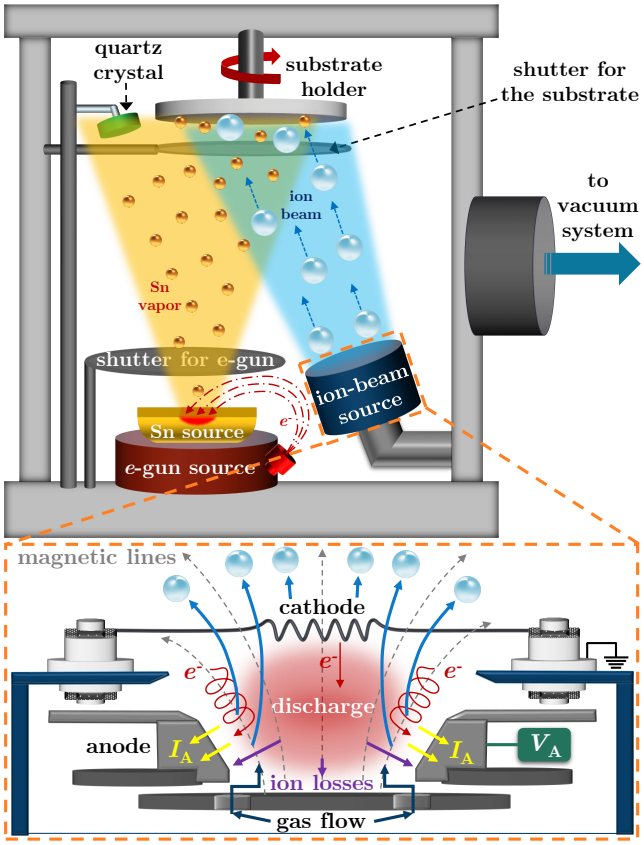

Figure 1. The schematic components of the IBAD system. Inset (orange-dashed rectangle): schematic of the working mechanism of the gridless (end-Hall) ion-beam source.

7.2×10^{17} cm^{-3} (see Fig. 2(b)), can be obtained by using a low I_A of 0.2 A and varying the percentage of OFR (O_2/(O_2+Ar)) from 8.57% to 14.29%. Subsequently, the *n*-type conductivity can be achieved by using a higher I_A of 0.4 A and an OFR of greater than 42%, as shown by Figs. 2(c) and (d). However, outside of these two regions (the shaded areas), Hall measurements could not be performed due to the increased resistivity of the film above the instrument's measuring limit. This argument is elaborated by the resistance value, obtained through the Ohmic $I-V$ measurement (see Fig. S1), which drastically increases by about 6 orders as soon as the OFR is increased above 15%. This region of high resistivity is called the conductivity dilemma area because it shows neither *p*-type nor *n*-type conductivity consistently.[25,45] Hall measurements for SnO films with an anode current of 0.3 A also fall into this dilemmatic area and therefore cannot be presented here.

The low/high anode currents used to obtain *p*-type/*n*-type SnO_x films, respectively, are associated with the density of the energetic ions generated by the ion-beam source, as illustrated in the inset of Fig. 1 (orange-dashed rectangle). In a Hall-end ion source,[46] the electrostatic discharge is under the influence of a magnetic field, causing the electrons to move towards the anode in a helical fashion where the magnetic and electric fields intersect. The circularly moving electrons increase their residence time in the plasma before arriving at the anode, thereby allowing sufficient impact ionization of the electrons to balance the loss of ions.[47] They collide with the incoming gas molecules and form ions, which eventually escape towards the cathode following the electric-field lines. From this view, one can perceive that the number of electrons captured at the anode, *i.e.*, the anode current I_A, will determine the number of ions emitted by the ion gun.[47] Even if the gas flow rate continues to increase, there will be a saturation of the number of ionized oxygen ions. Since stoichiometrically SnO has less oxygen than SnO_2, the deposition of SnO will require a lower anode current than SnO_2 to reach its stoichiometry. This explains why *p*-type films were obtained at a lower I_A of 0.2 A, whereas *n*-type films were obtained at a higher I_A of 0.4 A. This description is also consistent with the observed conductivity dilemma for SnO_x films with $I_A = 0.3$ A. Most likely, this current produces an ion density that is stoichiometrically between SnO and SnO_2, so the resistivity of the resulting film is too high for Hall measurements.

Figures 2(b) and (d) (right axis) show the corresponding optical characteristics of the SnO_x films. The optical bandgap of the film was retrieved from the transmission spectrum using a Tauc plot, as shown in Fig. S2. Overall, the optical bandgap of the SnO_x films gradually increases with increasing OFR, indicating an improved oxidation process in the films. The bandgap of the *p*-type SnO_x films (OFR of 8.57% to 14.29%) ranges from 2.10 eV to 2.42 eV, which is slightly narrower than the typical SnO bandgap (~2.70 eV[10,23,25]). This indicates that the *p*-type film is formed non-stoichiometrically under Sn-rich conditions, which is also reflected in its low film transmission below 37% (see Fig. S2(a)). A higher bandgap can be achieved when the OFR is further increased, but the electrical properties fall into the conductivity dilemma area. Furthermore, the bandgaps for the *n*-type films (OFR of 42.86% to 48.57%) range from 3.59 eV to 3.63 eV, which closely matches the bandgaps of *n*-type SnO_2 films in the literature.[25,36] In addition, the transmission of the film is also greatly increased to over 70% (see Fig. S2(c)). It appears that suitable optical characteristics have been achieved for the *n*-type films. However, their *p*-type counterparts still need to be further optimized, which will be discussed later in Fig. 3.

Raman scattering spectroscopy was used to identify the Raman-active phonon modes of the films, which could be used to analyze their microstructure. In Figs. 2(e) and (g), we map the frequency of the SnO and SnO_2 Raman-active modes (see Fig. S3) on the Raman spectra of SnO_x films prepared by $I_A = 0.2$ A and $I_A = 0.4$ A, respectively. The Raman spectrum for an air-annealed sample is also included as a reference (black line). For the annealed sample, the two peaks associated with the SnO A_{1g} and B_{1g} modes are visible at the frequencies of ~210 cm^{-1} and ~110 cm^{-1}, respectively.[23,45,48] In addition, a broad peak at ~385 cm^{-1} was also observed, which can be attributed to the formation of SnO_2 surface defects.[49] However, for the as-deposited samples, no significant microstructure phase was detected. The SnO_x film with an OFR of 8.57% did show Raman peaks in the A_{1g} and B_{1g} modes, but the signal was very low compared to the reference sample and dropped drastically for an OFR of over 11.43%. Likewise, for the SnO_2 vibration mode, there was no significant signature indicating the formation of SnO_2 microcrystals in the film for all OFR variations using both $I_A = 0.2$ A and $I_A = 0.4$ A. Thus, the structure of the SnO_x films deposited by the IBAD technique can be either amorphous or nanocrystalline. Figures 2(f) and (h) show the surface morphology of the samples prepared by the low I_A (OFR = 14.29%) and the high I_A (OFR = 42.86%), respectively. The FE-SEM images reveal that the surface

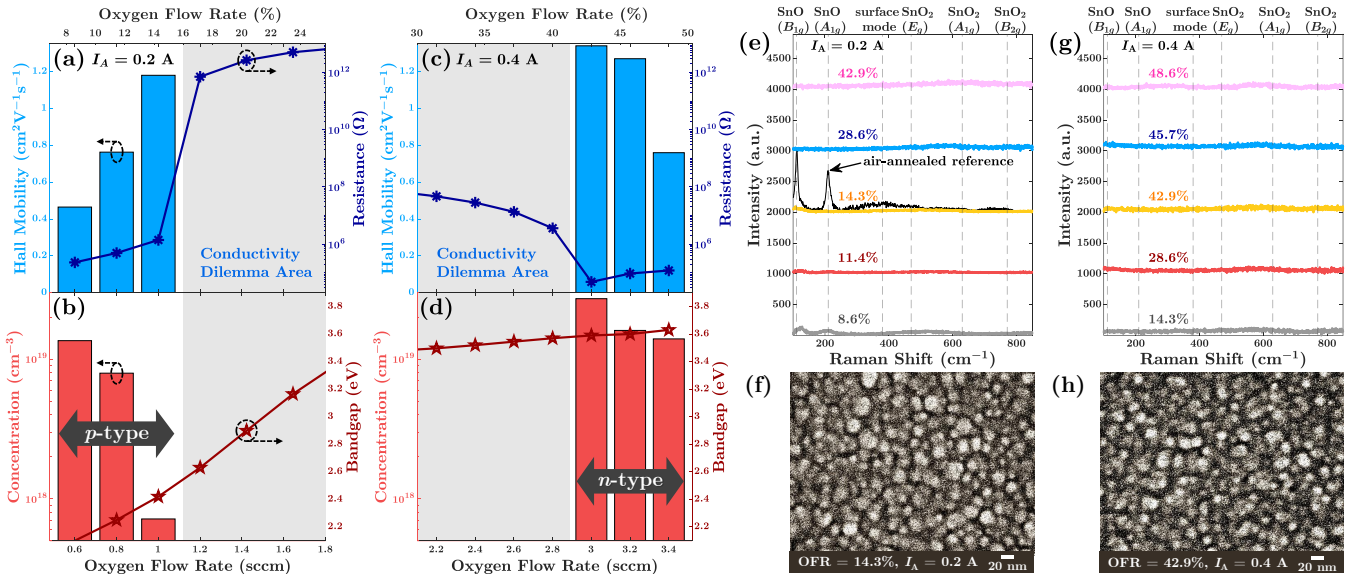

Figure 2. The evolution of (a, c) Hall mobility (left axis) and Ohmic resistance (right axis) and (b, d) carrier concentration (left axis) and optical bandgap (right axis) of the SnO_x films corresponds to variations in the OFR (the TFR of O_2 and Ar was set at 7.0 sccm) at anode currents of 0.2 A and 0.4 A (V_A = 180 V), respectively. Note that the Hall mobility and hole concentration are the averages of six different experiments. Raman scattering spectra for the SnO_x films prepared by (e) I_A = 0.2 A and (g) I_A = 0.4 A with different OFRs. FE-SEM images of representative SnO_x films prepared using (f) a low I_A (OFR = 14.29%) and (h) a high I_A (OFR = 42.9%). FE-SEM at a 100 nm scale is shown in Fig. S4.

Table 1. Summary of Hall mobility and hole concentrations of *p*-type SnO thin films fabricated using various deposition techniques at low temperatures ($\leq$ 100 °C) without involving post-deposition annealing. Note that the results shown here are for nanocrystalline films.

Deposition technique	Hall mobility ($cm^2V^{-1}s^{-1}$)	Hole concentration ($\times10^{16}$ cm^{-3})	Ref.
IBAD	7.89[a]	4.9	**this work**
	4.57[b]	35.6	
	1.18[c]	71.6	
DC sputtering	5.11	0.1	Jung et al.[17]
e-beam evaporation	2.60	500.0	Guo et al.[27]
	1.00	140.0	
RF sputtering	1.08	6.2	Yang et al.[28]
RF sputtering	0.47	56,500.0	Ahn et al.[50]
RF sputtering†	0.02	1,470.0	Um et al.[51]
atomic layer deposition†	1.39	39,500.0	Kim et al.[5]

[a] OFR = 1.0 sccm & TFR = 6.0 sccm
[b] OFR = 0.8 sccm & TFR = 6.0 sccm
[c] OFR = 1.0 sccm & TFR = 7.0 sccm
† plus heating the substrate at 100 °C during deposition

structure of the SnO_x films is most likely nanocrystalline, as indicated by the nanocrystal grains having an average diameter of 23.8 nm.

To optimize the *p*-type conductivity in the SnO_x films, we took a finer tuning of the OFR by lowering the total flow rate (TFR) of Ar and O_2 from 7.0 sccm to 6.0 sccm. Slightly reducing the dilution of the inert Ar gas will make the oxygen in the ion source slightly more reactive, but not so much as to maintain a low cathode erosion rate.[46,52,53] Figure 3(a) shows the Hall mobility and carrier concentration in the SnO sample prepared using I_A = 0.2 A and OFR = 0.4−1.0 sccm at the TFR of 6.0 sccm. Similar to the previous cases (Figs. 2(a) and (b)), an increase in OFR leads to an increase in Hall mobility along with a decrease in carrier concentration. The difference is that, by using 1.0 sccm OFR, now the mobility of SnO_x films can be boosted up to 7.89 $cm^2V^{-1}s^{-1}$. Remarkably, as summarized in Table 1, this is the highest mobility recorded for the *p*-type SnO films prepared entirely at room temperature. By lowering the TFR to 6.0 sccm, the 1.0-sccm OFR accounted for 16.7% of the TFR, thereby contributing approximately 2.4% more oxygen ions to oxidize the film than in the previous case. As compared in Table 1, this addition of oxygen ions succeeded in lowering the carrier concentration from 71.6×10^{16} cm^{-3} to 4.9×10^{16} cm^{-3}, leading to an increase in the mobility possibly by reducing the scattering effect of the ionized impurity.[12,54] Moreover, Figure 3(b) shows that the optical transparency of the SnO_x film increased up to 50.5% and the optical bandgap also increased to 2.70 eV (see the inset figure), which is now in good agreement with the literature.[10,23,25] Interestingly, the Raman spectra in Figure 3(c) show that the enhanced *p*-type samples retain similar nanostructures to those using the 7.0-sccm TFR shown earlier (Figs. 2(e) and (f)). The Raman signal is dominated by two small and broad peaks of the B_{1g} and A_{1g} modes, located at 123.0 cm^{-1} and 207.0 cm^{-1}, respectively. Since the B_{1g} and A_{1g} modes should be at 110 cm^{-1} and 210 cm^{-1} for the highly crystalline SnO films,[23,45,48] the weak and slightly shifted signals confirm that the SnO_x films are composed of disordered nanocrystals.

In order to understand the mechanism underlying the *p*-type conductivity in the room-temperature-fabricated SnO_x films, we performed first-principle calculations based on the density functional theory (see the Supporting Information for the details). Figure 3(d) indicates that excess Sn atoms in SnO can form a hole-transport pathway through the overlapping Sn−Sn orbitals. The Sn interstitial can promote more Sn−Sn overlap, which bridges the charge-density dis-

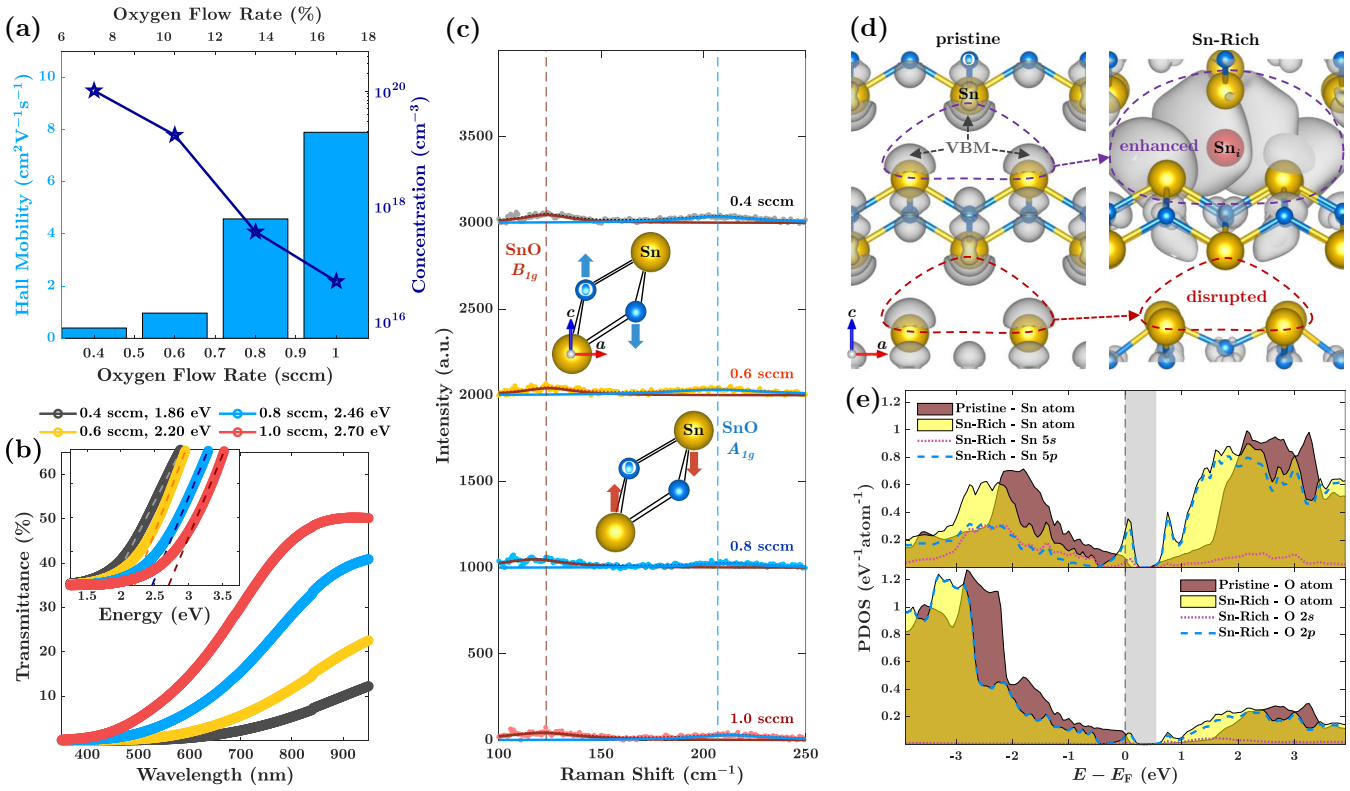

Figure 3. Hall mobility (left axis) and carrier concentrations (right axis) of the SnO_x films as functions of OFR. (b) The corresponding transmittance spectrum and Tauc plot (inset). (c) The deconvolution of the A_{1g} and B_{1g} peaks in the Raman scattering spectra of the SnO_x films with varying OFR. (d) Comparison of the spatial distribution of SnO VBM states between pristine and Sn-rich conditions. (e) Partial density of states of the Sn atom (upper panel) and the O atom (lower panel) for the pristine SnO and the Sn-rich SnO.

tribution between the layered structures. Such overlapping helps to expand the isosurface of the VBM state and form a continuous transport path, so the holes can move more easily between the SnO interlayers. The role of excess Sn atoms in modifying orbital interactions in the VBM state can be further understood by examining the change of the partial density of states (PDOS) of SnO upon addition of a Sn interstitial into the SnO matrix, as shown in Fig. 3(e). When a Sn interstitial is added, the states of the Sn 5*p* orbitals increase around the VBM (see the upper panel). As suggested by Alshareef and coworkers, the increase in the Sn 5*p* state was the source of the high mobility observed in Sn-rich SnO films,[33] which were reported to reach 18.7 $cm^2V^{-1}s^{-1}$ after careful control of oxygen partial pressure and annealing conditions.[14]

However, the stabilization of the excess Sn atom inherently comes at the cost of lattice distortion, which could result in disruption of the transport pathway. As shown in Fig. 3(d) (right panel), the enhanced orbital overlaps in the layer with Sn_i perturbing the VBM isosurface in the neighboring layer. The Sn−Sn bonds in the neighboring interlayer must be distorted to stabilize the Sn_i location between the lattice sites. This behavior suggests that increasing Sn_i, in addition to aiding hole transport, also induces more lattice distortion, which may counteract its mobility-enhancing effect. In other words, the hole mobility will decrease with increasing distortion in the crystal structure, explaining why the *p*-type conductivity was not detected in the fully amorphous films in previous reports.[18,29,30] Thus, this theory provides insight that *p*-type transport can be achieved in room-temperature processes by carefully controlling the number of excess Sn atoms to strike a balance between overlapping Sn−Sn orbitals and lattice distortion.

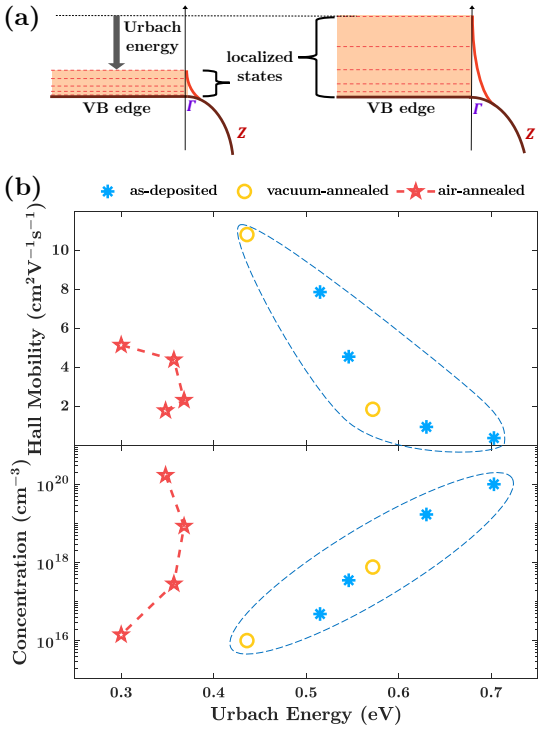

Figure 4. (a) Schematic representation of the decrease in Urbach energy. (b) Summary of Hall mobility (upper panel) and hole concentration (lower panel) as functions of Urbach energy.

By using absorption spectroscopy, information related to

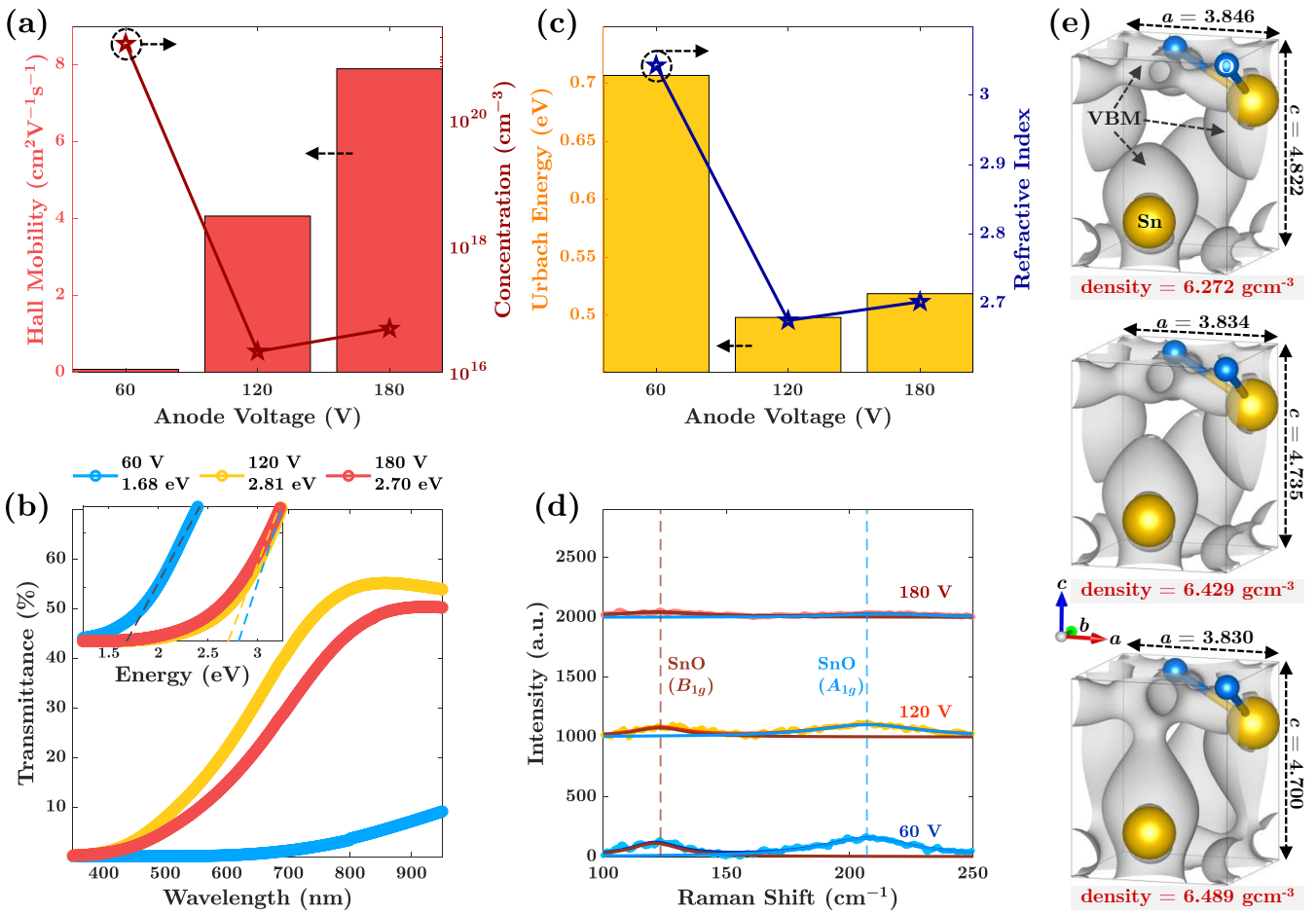

Figure 5. (a) Hall mobility (left axis) and carrier concentrations (right axis) of the SnO_x thin films with anode-voltage variations. (b) The corresponding transmittance spectra and Tauc plot (inset). (c) Urbach energy (left axis) and refractive index (right axis) as functions of anode voltage. (d) Raman scattering spectra for the SnO_x films with varying anode voltage. (e) Spatial distribution of VBM states for SnO unit cells with different cell densities. Here the different densities shown from left to right panels, respectively, are generated by applying pressures of 0.5, 1.5, and 2 GPa in the cell-relaxation process.

the degree of lattice disorder in SnO films can be evaluated through a parameter called Urbach energy. As illustrated in the band diagram in Fig. 4(a), the decrease in Urbach energy reflects a lower localized state due to the reduced degree of disorder in the SnO lattice. Figure 4(b) shows the evolution of mobility and concentration with respect to changes in the Urbach energy. According to the theoretical predictions given in Figs. 3(d) and (e), in addition to increasing the metal's contribution to VBM, increasing Sn_i has an impact on increasing lattice distortion and shifting the Fermi level into VB. This indicates that an increase in the Sn content will be accompanied by a decrease in mobility and an increase in carrier concentration. This behavior is in line with the trend shown in the experimental data in Fig. 4(b), i.e., the trend of increasing mobility and decreasing carrier concentration coincides with a decrease in Urbach energy. Here, OFR plays an important role in controlling the O/Sn ratio to achieve a balance between Sn−Sn overlap and structural disturbances. As shown by the EDS data in Fig. S5, the O/Sn ratio increased from 0.759 to 0.889 when the OFR was increased from 0.6 sccm to 1.0 sccm. One can see that the decrease in Urbach energy is related to the decrease in the number of Sn atoms. Thus, it is consistent that an increase in mobility is closely related to a decrease in lattice distortion caused by the Sn-rich-associated defects, such as Sn interstitials.

In addition to the OFR, the anode voltage of the ion-gun, V_A, plays a key role in controlling the kinetic energy of the incoming ions,[46,52] which greatly affects the oxidation of the Sn vapors.[43,44] As shown by Figs. 5(a) and (b), the quality of the *p*-type SnO_x film becomes more optimal, both electrically and optically, when the anode voltage is adjusted properly. Using a low V_A of 60 V, the hole mobility is only 0.07 $cm^2V^{-1}s^{-1}$, which is followed by a very high carrier concentration of 1.6×10^{21} cm^{-3} (see Fig. 5(a)). In addition, the transmittance and bandgap of the film are, respectively, low below 10% (Fig. 5(b)) and narrow at 1.68 eV (the inset figure), resulting in a highly reflective/absorbent film. By increasing the V_A to 120 V, the mobility increases to 4.06 $cm^2V^{-1}s^{-1}$, and ultimately reaches the highest mobility of 7.89 $cm^2V^{-1}s^{-1}$ at the V_A of 180 V. The films also exhibit about 5-fold higher transparency and much higher energy gaps of 2.81 eV and 2.70 eV for the V_A of 120 V and 180 V, respectively. Notably, the latter yields a bandgap value that agrees with the literature (2.70 eV).[10,23,25] Therefore, the anode voltage of 180 V provides a more optimal film quality by achieving the highest mobility and proper optical bandgap.

A sufficiently high anode voltage can induce a more energetic ion flux, which allows more efficient oxidation of Sn metal at room temperature through the ion-bombardment process.[43,44] The oxidation can be seen from the optical

transparency of the film that increases significantly when the V_A is increased from 60 V to 120 V. This behavior is also corroborated by the Urbach energy and refractive index of the film given in Fig. 5(c), which decreased drastically from 0.707 eV to 0.498 eV and from 3.04 to 2.68, respectively. The substantial decrease in the Urbach energy and refractive index is a strong indication that the incorporation of oxygen ions to the Sn metal is enhanced. Therefore, the increased mobility in this range can be attributed to a significant reduction in the localized state due to the enhanced oxidation process. By increasing the potential further, the kinetic energy of the bombarding ions will continue to increase so that the oxidation process will be followed by film densification.[43,52] This trend can be observed at the V_A of 180 V, where there is a slight increase in the Urbach energy and refractive index to 0.519 eV and 2.7, respectively. The densification of the SnO microstructure is also revealed by the Raman spectra, as shown in Fig. 5(d). One can see that the intensity of the SnO B_{1g} and A_{1g} modes decreases slightly when V_A is increased to 120 V, and then decreases substantially when V_A reaches 180 V. Therefore, the high anode voltage is responsible for the SnO films whose microstructure tends to be nanocrystalline.

We speculate that the densification of the SnO microstructure (by imposing the V_A of 180 V) reduces the distance between the SnO layers, thereby promoting more Sn−Sn overlap and further enhancing the mobility of the holes. This hypothesis is supported by a reduction in the bandgap from 2.81 eV and 2.70 eV when the V_A is increased from 120 V to 180 V (see Fig. 5(b)). It has been studied very recently that reducing the Sn−Sn interlayer tends to reduce the optical bandgap.[39,55] To illustrate the effect of crystal densification on overlapping Sn−Sn orbitals, we show the spatial distribution of VBM states for SnO unit cells with different densities in Fig. 5(e). As the cell density increases, the isosurfaces of the VBM state are more widespread and become closer to the VBM state of their neighboring Sn interlayer.

To highlight the different characteristics of the films fabricated with and without an annealing procedure *via* the IBAD, we carried out post-annealing procedures at 250 °C for 30 min under vacuum and air conditions. Figure 6 compares the Hall mobility and the corresponding hole concentrations as functions of OFR between the as-deposited and the annealed samples. Using vacuum annealing, the mobility of the 0.8-sccm-OFR sample could be increased further from 4.57 $cm^2V^{-1}s^{-1}$ to 10.84 $cm^2V^{-1}s^{-1}$ thanks to a significant reduction in carrier concentration from 3.6×10^{17} cm^{-3} to 1.0×10^{16} cm^{-3}. However, the 1.0-sccm-OFR sample carrier concentration became too low (too high resistivity) to be detected by Hall-effect measurements. In addition, the 0.4-sccm-OFR sample also showed no p-type conductivity. This is most likely because the annealing process takes place in very poor oxygen conditions so that the metallic properties become more dominant.[43] As a result, the process window becomes narrower when vacuum annealing is involved. Interestingly, Figure 4(b) (orange dots) indicates that the trend of mobility, carrier concentration, and Urbach energy still holds for the vacuum-annealed samples. This is because the vacuum-annealed films retain optical characteristics and microstructure similar to that of the deposited films (see Figs. S8 and S9).

In contrast, the air-annealed films exhibit somewhat different electrical characteristics (see Fig. 4(a) (red stars)). On the one hand, the characteristics of the mobility and

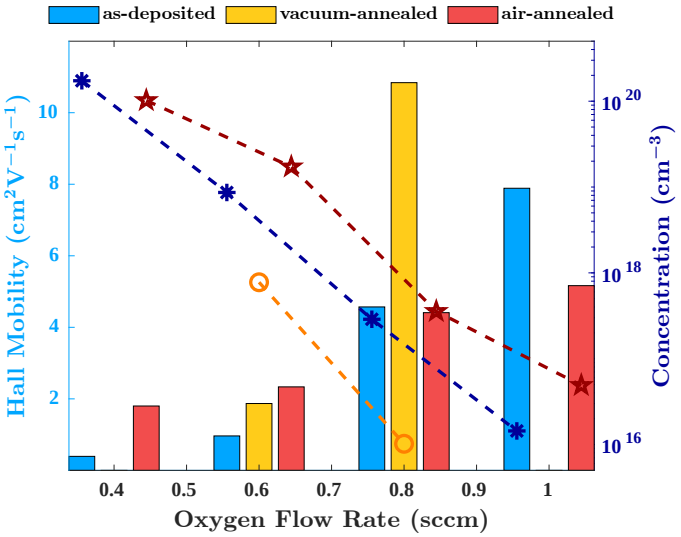

Figure 6. Comparison of Hall mobility (left axis) and carrier concentrations (right axis) as a function of OFR for SnO_x thin films under as-deposited and annealed in vacuum and air.

concentration of holes, which increase and decrease with increasing OFR, respectively, are still maintained. Thus, the dependence of the p-type conductivity on the O/Sn ratio may still hold in this sample. However, even though the Urbach energy drops drastically to 0.300 eV, the resulting optimal mobility is only 5.17 $cm^2V^{-1}s^{-1}$. This value is lower than that of the as-deposited and vacuum-annealed films, both of which have higher Urbach energies . This distinctive behavior suggests that there is an additional contribution to limiting the hole mobility in the air-annealed film. Figure 7(a) shows that, despite having a higher transmittance (the inset), the optical bandgap of the air-annealed films varies between 2.84 eV and 2.97 eV. These values slightly deviate from the SnO bandgap and, in fact, are closer to the Sn_3O_4 optical gap (2.95 eV).[56] This suggests that the intermediate phase co-formed with the SnO phase in the air-annealed samples, which might be the source for their different p-type characteristics. The signature of the phase transformation can be elaborated by examining the refractive index of the films.[30] Figure 7(b) shows a decreasing trend of n_F concomitant with the transition of conductivity from p-type to n-type. This behavior mimics a phase transformation from SnO to SnO_2.[30] The n_F-values of the as-deposited and vacuum-annealed SnO_x films are greater than those of the air-annealed films. In good agreement with the literature,[25,30,57] the refractive indices of the p-type SnO films are much larger than those of the n-type films; for example, compared to those prepared using OFRs higher than 3 sccm and $I_A = 0.4$ A (see the inset figure). The refractive indices of the p-type films range from 2.70 - 2.97, while the n-type samples have a much lower refractive index of only ∼2.34. For the air-annealed samples, their refractive index lies between these two values, which is ∼2.66. The decrease in the n_F value of the air-annealed film towards the refractive index of SnO_2 corroborates that the SnO phase is in the process of transforming to SnO_2 through the intermediate phase.[30,36,37]

Figure 7(c) shows the Raman shift of the air-annealed films, which can be deconvoluted by four Raman vibration modes: A_{1g}, B_{1g}, and two $SnO_{1<x<2}$ intermediate modes. The presence of these multiple intense peaks indicates the

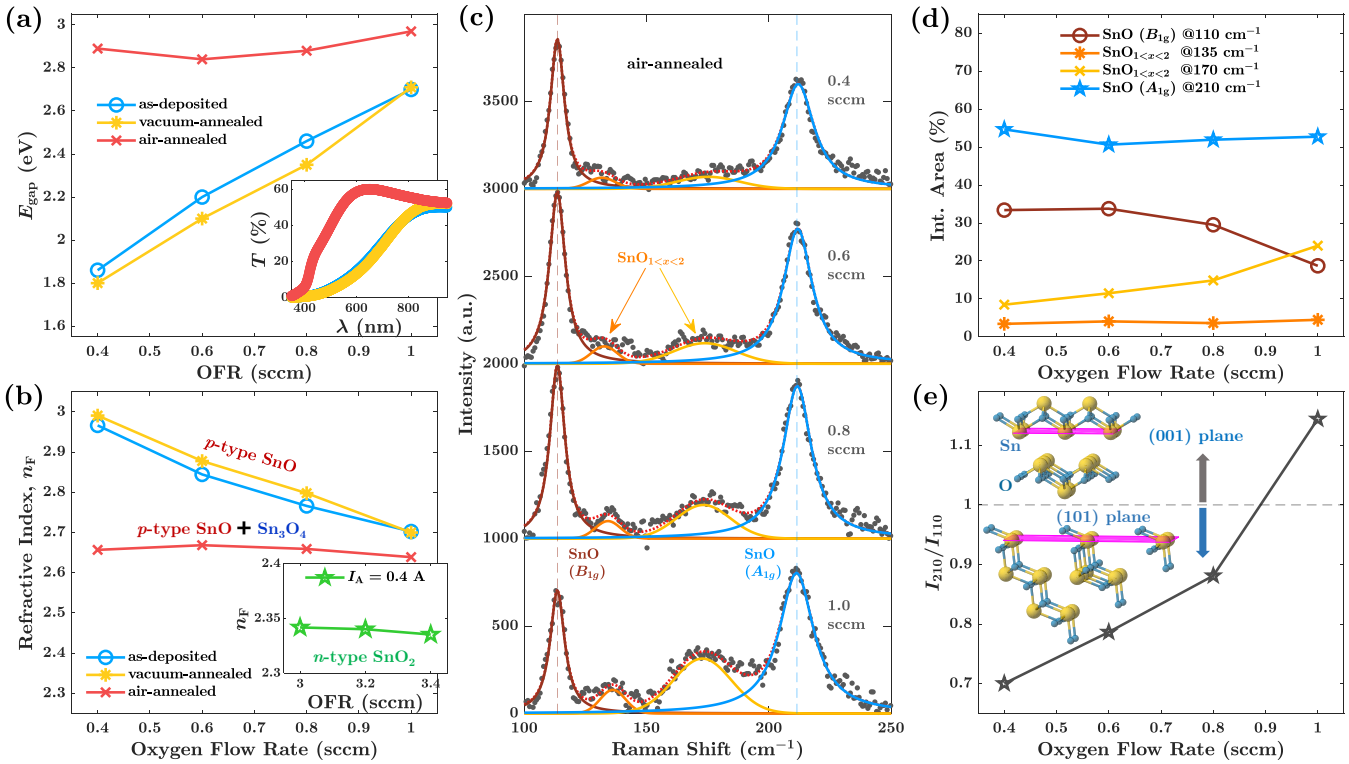

Figure 7. The optical bandgap as a function of OFR for each preparation condition. Inset: comparison of the transmittance spectra for the 1.0-sccm-OFR films under as-deposited, vacuum-annealed, and air-annealed conditions. (b) Changes in the Moss refractive index to the increase in OFR. Inset: the results for the n-type SnO_2 films prepared using higher OFRs and $I_A = 0.4$ A. (c) The deconvolution of the A_{1g}, B_{1g}, and $SnO_{1<x<2}$ peaks in the Raman scattering spectra of SnO_x films under air-annealed conditions at varying OFRs. (d) Relative total area of the deconvoluted Raman peaks. (e) Evolution of the intensity ratio of A_{1g} (~210 cm^{-1}) and B_{1g} (~110 cm^{-1}) modes with respect to an increase in OFR.

formation of microcrystals of the SnO phase and the Sn_3O_4 intermediate phase, which is in line with the predictions deduced from the optical characteristics. The intensity of the A_{1g} mode continues to increase as the OFR increases from 0.6 sccm to 1.0 sccm. Also, the A_{1g} mode shifts approaching 211.0 cm^{-1} as the OFR increases, which gets close to the Raman frequency of highly crystalline SnO films.[23,45,48] During the annealing treatment in ambient air, oxygen molecules from the environment are adsorbed onto the surface of the SnO thin film due to the presence of additional heat energy and obtain higher surface diffusion, thereby causing lattice relaxation and increased crystallization.[58,59] Unfortunately, the increase in crystallization is followed by an increase in the intermediate phase. The two sub-stoichiometric $SnO_{1<x<2}$ phases lying between the A_{1g} and B_{1g} modes are promoted when more oxygen is introduced into the SnO layer. The lower-frequency intermediate mode shifted its peak position from 131.7 cm^{-1} to 136.2 cm^{-1}, while the higher-frequency mode shifted from 175.2 cm^{-1} becomes 172.8 cm^{-1}. The positions of the two peaks become closer to 145.0 cm^{-1} and 171.0 cm^{-1}, respectively, which matches most of the SnO_x intermediate-phase phonon modes in the previously reported SnO films.[23,48] The formation of the intermediate phase is most likely the cause of the limited electrical performance of the air-annealed sample.

To examine the distribution of these phases against changes in OFR, we display the relative percentage of the integrated area of each mode in Fig. 7(d). The relative area of the A_{1g} mode dominates about 50% of the total signal and the percentage hardly changes with increasing OFR, so this is a strong indication that the SnO microstructure is formed in all the air-annealed samples. The low-frequency intermediate phase (~135 cm^{-1}) shows a less significant contribution because its relative area is about 4% with an unchanged trend towards increasing OFR. However, there is an interplay between the B_{1g} mode and the high-frequency intermediate mode (~170 cm^{-1}). When the OFR is increased, the B_{1g} mode attenuates from 33% to 19% while the intermediate phase increases from 9% to 24%. This situation reflects the decomposition of the B_{1g} mode into a SnO_x intermediate phase. Hence, there is a competition between the formation of the SnO A_{1g} phase and the decomposition of the B_{1g} phase into a SnO_x intermediate phase.

The impact of decomposition of the B_{1g} phase into an intermediate phase on the microstructure of the film can be analyzed by evaluating the peak area ratio of A_{1g} and B_{1g} peaks, as shown in Fig. 7(e). As reported by Liu *et al.*,[22] the vibrational modes at A_{1g} and B_{1g}, respectively, are closely related to the grain orientation of the (001) and (101) planes in the SnO litharge structure. Hence, the intensity ratio of the A_{1g} mode (~210 cm^{-1}) and B_{1g} mode (~110 cm^{-1}), I_{210}/I_{110}, can be associated with the relative texture coefficient between the (001) and (101) grain orientations (see the inset figure). Ratio values less than one correspond to the (101) plane orientation, while values above one correspond to the (001) plane orientation. Changes in grain orientation can cause an increase in grain boundary in the film. This factor could be the additional scattering effect for the hole carriers, thereby limiting the increased mobility of the air-annealed sample.

Finally, we fabricated p-n diodes based on the SnO films (~125 nm thickness) and evaluated the evolution of the $I-V$

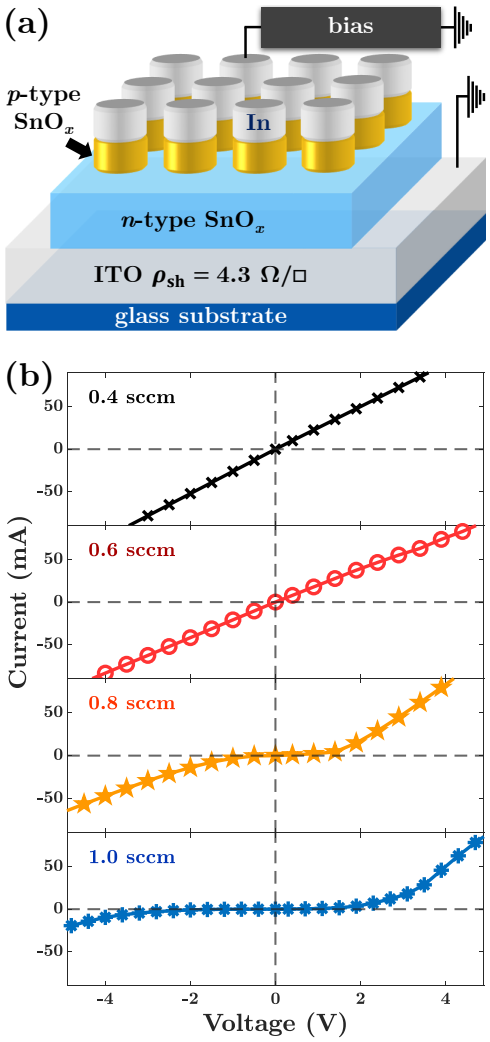

Figure 8. (a) Schematic of the SnO_x-based *p*-*n* diodes. (b) Current-voltage measurement for the *p*-*n* junction using *p*-type samples with different OFRs.

characteristics to the OFR changes in the *p*-type layer. For the *n*-type layer, we used the most optimal recipe based on the OFR of 42.86%, I_A = 0.4 A, and a thickness of ∼150 nm. The device structure is shown in Fig. 8(a). Figure 8(b) shows the rectifier characteristics of the *p*-*n* diode with respect to changes in OFR. Devices prepared with OFRs of 0.4 sccm and 0.6 sccm does not reveal their diode characteristics, but instead exhibits Ohmic curves similar to probing *n*-type films (see the top two panels in Fig. 8(b)). This behavior mainly arises due to the abundance of Sn metal in the SnO matrix, as revealed by the EDS data showing O/Sn less than 0.760 (Fig. S5). A rectifier character begins to appear in the diode prepared with an OFR of 0.8 sccm, indicating the presence of a well-formed *p*-type layer in the device. The junction between the *p*- and *n*-type layers induces a depletion layer at the interface as a result of the recombination of holes from the *p*-type side and electrons from the *n*-type side, which eventually forms a built-in potential that leads to the diode characteristics. The most optimal rectifier characteristic is achieved on the device with an OFR of 1.0 sccm (bottom panel). This diode can withstand reverse bias from 0 to -3 V, which is higher than the device with an OFR of 0.8 sccm (only last up to -1 V). The device is also improved compared to that prepared with a TFR of 7.0 sccm (see Fig. S6), where the reverse bias only persists to about -1 V. These aspects confirm the improvement of the *p*-type conductivity of the SnO_x films, which is in line with the Hall measurements. Thus, the IBAD technique is highly capable of producing *p*-*n* devices, which is remarkable considering that these devices were fabricated without an annealing procedure.

We have successfully demonstrated the fabrication of *p*-type SnO_x thin films with an excellent electrical performance at room temperature using the IBAD technique. The optimal *p*-type SnO film exhibited Hall mobility, hole concentration, and optical transparency (gap energy) of 7.89 $cm^2V^{-1}s^{-1}$, 4.9×10^{16} cm^{-3}, and 50.5% (2.70 eV), respectively. This performance was achieved using an OFR of 1.0 sccm ($O_2/(O_2+Ar)$ = 1/6), anode current of 0.2 A, anode voltage of 180 V, and deposition rate of 0.3 $Å s^{-1}$. In the IBAD system, the anode voltage of the ion-gun has a significant effect on increasing the performance of the *p*-type SnO film. By controlling the anode voltage, we can increase the Hall mobility from 0.07 $cm^2V^{-1}s^{-1}$ to 7.89 $cm^2V^{-1}s^{-1}$ without having to go through an annealing process that tends to introduce microcrystals into the film. As revealed by Raman scattering, there were no significant signs of microcrystal formation in all the as-deposited films. In contrast, when the annealing method was carried out on the SnO_x samples in an air environment, crystallization was formed and strengthened when the oxygen content increased. Unfortunately, this process was followed by the occurrence of SnO_x intermediate phases, which tend to be carrier compensators. As a result, the optimal mobility of the film was reduced to 5.17 $cm^2V^{-1}s^{-1}$. Additionally, we were able to show that the IBAD method could facilitate the fabrication of SnO_x-based *p*-*n* devices entirely at room temperature.

The above discussion shows that a full room-temperature process is more desirable for fabricating *p*-type SnO films. The Raman shift data indicate that the post-annealing process in the air is accompanied by complex phase transformations, leading to the diversified and difficult-to-control electrical performance of the SnO films. This is in line with many reports in the literature,[5,14,15] where precise control is required to obtain high-performance *p*-type SnO films. This study is expected to pave the way for preparing *p*-type oxide semiconductors fully at room temperature, which has very significant applications for realizing flexible, transparent, and giant electronics.

The Supporting Information is available free of charge on the ACS Publications website at `http://pubs.acs.org`.

The authors declare no competing financial interest.

Acknowledgement This work was supported and funded by the Ministry of Science and Technology Taiwan Project (109-2221-E-182-063-MY3, 109-2221-E-182-021-MY3) and the Chang Gung Memorial Hospital Research Project (CMRPD2M0031).

References

(1) Nomura, K.; Ohta, H.; Takagi, A.; Kamiya, T.; Hirano, M.; Hosono, H. Room-Temperature Fabrication of Transparent Flexible Thin-Film Transistors using Amorphous Oxide Semiconductors. *Nature* **2004**, *432*, 488–492.

(2) Zhong, M.; Zeng, W.; Liu, F.-S.; Fan, D.-H.; Tang, B.; Liu, Q.-J. Screening criteria for high-performance *p*-type transparent conducting materials and their applications. *Materials Today Physics* **2022**, *22*, 100583.

(3) Sheng, J.; Hong, T.; Lee, H.-M.; Kim, K.; Sasase, M.; Kim, J.; Hosono, H.; Park, J.-S. Amorphous IGZO TFT with High Mobility of ∼70 $cm^2/(Vs)$ *via* Vertical Dimension Control Using

PEALD. *ACS Applied Materials & Interfaces* **2019**, *11*, 40300–40309, PMID: 31584254.
(4) Fortunato, E.; Barquinha, P.; Martins, R. Oxide Semiconductor Thin-Film Transistors: A Review of Recent Advances. *Advanced Materials* **2012**, *24*, 2945–2986.
(5) Kim, H.-M.; Choi, S.-H.; Jeong, H. J.; Lee, J.-H.; Kim, J.; Park, J.-S. Highly Dense and Stable *p*-Type Thin-Film Transistor Based on Atomic Layer Deposition SnO Fabricated by Two-Step Crystallization. *ACS Applied Materials & Interfaces* **2021**, *13*, 30818–30825, PMID: 34156823.
(6) Liang, L. Y.; Tao Cao, H.; Bo Chen, X.; Min Liu, Z.; Zhuge, F.; Luo, H.; Li, J.; Cheng Lu, Y.; Lu, W. Ambipolar inverters using SnO thin-film transistors with balanced electron and hole mobilities. *Applied Physics Letters* **2012**, *100*, 263502.
(7) Hosono, H. Recent progress in transparent oxide semiconductors: Materials and device application. *Thin Solid Films* **2007**, *515*, 6000–6014, Proceedings of Sympodium O on Thin Film Chalcogenide Photovoltaic Materials, EMRS 2006 Conference.
(8) Schein, F.-L.; Winter, M.; Böntgen, T.; von Wenckstern, H.; Grundmann, M. Highly rectifying *p*-$ZnCo_2O_4$/*n*-ZnO heterojunction diodes. *Applied Physics Letters* **2014**, *104*, 022104.
(9) Togo, A.; Oba, F.; Tanaka, I.; Tatsumi, K. First-principles calculations of native defects in tin monoxide. *Physical Review B* **2006**, *74*, 195128.
(10) Ogo, Y.; Hiramatsu, H.; Nomura, K.; Yanagi, H.; Kamiya, T.; Hirano, M.; Hosono, H. *p*-channel thin-film transistor using *p*-type oxide semiconductor, SnO. *Applied Physics Letters* **2008**, *93*, 32113.
(11) Minohara, M.; Hase, I.; Aiura, Y. Characteristic Electronic Structure of SnO Film Showing High Hole Mobility. *The Journal of Physical Chemistry Letters* **2022**, *13*, 1165–1171, PMID: 35084204.
(12) Minohara, M.; Samizo, A.; Kikuchi, N.; Bando, K. K.; Yoshida, Y.; Aiura, Y. Tailoring the Hole Mobility in SnO Films by Modulating the Growth Thermodynamics and Kinetics. *The Journal of Physical Chemistry C* **2020**, *124*, 1755–1760.
(13) Miller, S. A.; Gorai, P.; Aydemir, U.; Mason, T. O.; Stevanović, V.; Toberer, E. S.; Snyder, G. J. SnO as a potential oxide thermoelectric candidate. *Journal of Materials Chemistry C* **2017**, *5*, 8854–8861.
(14) Caraveo-Frescas, J. A.; Nayak, P. K.; Al-Jawhari, H. A.; Granato, D. B.; Schwingenschlögl, U.; Alshareef, H. N. Record mobility in transparent *p*-type tin monoxide films and devices by phase engineering. *ACS Nano* **2013**, *7*, 5160–7.
(15) Fortunato, E.; Barros, R.; Barquinha, P.; Figueiredo, V.; Park, S.-H. K.; Hwang, C.-S.; Martins, R. Transparent *p*-type SnO_x thin film transistors produced by reactive rf magnetron sputtering followed by low temperature annealing. *Applied Physics Letters* **2010**, *97*, 052105.
(16) Minohara, M.; Kikuchi, N.; Yoshida, Y.; Kumigashira, H.; Aiura, Y. Improvement of the hole mobility of SnO epitaxial films grown by pulsed laser deposition. *Journal of Materials Chemistry C* **2019**, *7*, 6332–6336.
(17) Jung, J.; Park, S.; Ye, J.; Woo, J.; Bae, B.; Yun, E.-J. Optical, structural, and electrical properties of sputter-deposited SnO_x thin films. *Thin Solid Films* **2022**, *747*, 139139.
(18) Wahila, M. J. et al. Lone-Pair Stabilization in Transparent Amorphous Tin Oxides: A Potential Route to *p*-Type Conduction Pathways. *Chemistry of Materials* **2016**, *28*, 4706–4713.
(19) Wang, Z.; Nayak, P. K.; Albar, A.; Wei, N.; Schwingenschlögl, U.; Alshareef, H. N. Transparent SnO-SnO_2 *p*-*n* Junction Diodes for Electronic and Sensing Applications. *Advanced Materials Interfaces* **2015**, *2*, 1500374.
(20) Mameli, A.; Parish, J. D.; Dogan, T.; Gelinck, G.; Snook, M. W.; Straiton, A. J.; Johnson, A. L.; Kronemeijer, A. J. High-Throughput Atomic Layer Deposition of *p*-Type SnO Thin Film Transistors Using Tin(II)bis(tert-amyloxide). *Advanced Materials Interfaces* **2022**, *9*, 2101278.
(21) Ogo, Y.; Hiramatsu, H.; Nomura, K.; Yanagi, H.; Kamiya, T.; Kimura, M.; Hirano, M.; Hosono, H. Tin monoxide as an *s*-orbital-based *p*-type oxide semiconductor: Electronic structures and TFT application. *Physica Status Solidi A* **2009**, *206*, 2187–2191.
(22) Liu, Q.; Liang, L.; Cao, H.; Luo, H.; Zhang, H.; Li, J.; Li, X.; Deng, F. Tunable crystallographic grain orientation and Raman fingerprints of polycrystalline SnO thin films. *Journal of Materials Chemistry C* **2015**, *3*, 1077–1081.
(23) Geurts, J.; Rau, S.; Richter, W.; Schmitte, F. SnO films and their oxidation to SnO_2: Raman scattering, IR reflectivity and X-ray diffraction studies. *Thin Solid Films* **1984**, *121*, 217–225.
(24) Okamura, K.; Nasr, B.; Brand, R. A.; Hahn, H. Solution-processed oxide semiconductor SnO in *p*-channel thin-film transistors. *Journal of Materials Chemistry* **2012**, *22*, 4607.
(25) Luo, H.; Liang, L. Y.; Cao, H. T.; Liu, Z. M.; Zhuge, F. Structural, Chemical, Optical, and Electrical Evolution of SnO_x Films Deposited by Reactive rf Magnetron Sputtering. *ACS Applied Materials & Interfaces* **2012**, *4*, 5673–5677, PMID: 23025234.
(26) Toyama, T.; Seo, Y.; Konishi, T.; Okamoto, H.; Tsutsumi, Y. Physical Properties of *p*-Type Tin Monoxide Films Deposited at Low Temperature by Radio Frequency Magnetron Sputtering. *Applied Physics Express* **2011**, *4*, 071101.
(27) Guo, W.; Fu, L.; Zhang, Y.; Zhang, K.; Liang, L. Y.; Liu, Z. M.; Cao, H. T.; Pan, X. Q. Microstructure, optical, and electrical properties of *p*-type SnO thin films. *Applied Physics Letters* **2010**, *96*, 042113.
(28) Yang, T.; Zhao, J.; Li, X.; Gao, X.; Xue, C.; Wu, Y.; Tai, R. Preparation and characterization of *p*-type transparent conducting SnO thin films. *Materials Letters* **2015**, *139*, 39–41.
(29) Yabuta, H.; Kaji, N.; Hayashi, R.; Kumomi, H.; Nomura, K.; Kamiya, T.; Hirano, M.; Hosono, H. Sputtering formation of *p*-type SnO thin-film transistors on glass toward oxide complimentary circuits. *Applied Physics Letters* **2010**, *97*, 072111.
(30) Liang, L. Y.; Liu, Z. M.; Cao, H. T.; Yu, Z.; Shi, Y. Y.; Chen, A. H.; Zhang, H. Z.; Fang, Y. Q.; Sun, X. L. Phase and Optical Characterizations of Annealed SnO Thin Films and Their *p*-Type TFT Application. *Journal of The Electrochemical Society* **2010**, *157*, H598.
(31) Allen, J. P.; Scanlon, D. O.; Piper, L. F. J.; Watson, G. W. Understanding the defect chemistry of tin monoxide. *Journal of Materials Chemistry C* **2013**, *1*, 8194–8208.
(32) Chattopadhyay, D.; Queisser, H. J. Electron scattering by ionized impurities in semiconductors. *Rev. Mod. Phys.* **1981**, *53*, 745–768.
(33) Granato, D. B.; Caraveo-Frescas, J. A.; Alshareef, H. N.; Schwingenschlögl, U. Enhancement of *p*-type mobility in tin monoxide by native defects. *Applied Physics Letters* **2013**, *102*, 212105.
(34) Varley, J. B.; Schleife, A.; Janotti, A.; Van de Walle, C. G. Ambipolar doping in SnO. *Applied Physics Letters* **2013**, *103*, 082118.
(35) Kim, S. H.; Baek, I.-H.; Kim, D. H.; Pyeon, J. J.; Chung, T.-M.; Baek, S.-H.; Kim, J.-S.; Han, J. H.; Kim, S. K. Fabrication of high-performance *p*-type thin film transistors using atomic-layer-deposited SnO films. *Journal of Materials Chemistry C* **2017**, *5*, 3139–3145.
(36) Batzill, M.; Diebold, U. The surface and materials science of tin oxide. *Progress in Surface Science* **2005**, *79*, 47–154.
(37) Sarker, P.; Huda, M. N. Understanding the thermodynamic pathways of SnO-to-SnO_x phase transition. *Computational Materials Science* **2016**, *111*, 359–365.
(38) Jia, J.; Sugane, T.; Nakamura, S.-i.; Shigesato, Y. *p*-type conduction mechanism in continuously varied non-stoichimetric SnO_x thin films deposited by reactive sputtering with the impedance control. *Journal of Applied Physics* **2020**, *127*, 185703.
(39) Zhou, W.; Umezawa, N. Band gap engineering of bulk and nanosheet SnO: an insight into the interlayer Sn−Sn lone pair interactions. *Phys. Chem. Chem. Phys.* **2015**, *17*, 17816–17820.
(40) Husein, S.; Medvedeva, J. E.; Perkins, J. D.; Bertoni, M. I. The Role of Cation Coordination in the Electrical and Optical Properties of Amorphous Transparent Conducting Oxides. *Chemistry of Materials* **2020**, *32*, 6444–6455.
(41) Lee, S. J.; Jang, Y.; Kim, H. J.; Hwang, E. S.; Jeon, S. M.; Kim, J. S.; Moon, T.; Jang, K.-T.; Joo, Y.-C.; Cho, D.-Y.; Hwang, C. S. Composition, Microstructure, and Electrical Performance of Sputtered SnO Thin Films for *p*-Type Oxide Semiconductor. *ACS Applied Materials & Interfaces* **2018**, *10*, 3810–3821, PMID: 29322769.
(42) Song, S.-K. Characteristics of SnO_x films deposited by reactive-ion-assisted deposition. *Physical Review B* **1999**, *60*, 11137–11148.
(43) Choi, W.; Cho, J.; Song, S.; Jung, H.-J.; Koh, S.; Yoon, K.; Lee, C.; Sung, M.; Jeong, K. The characterization of undoped SnO_x thin film grown by reactive ion-assisted deposition. *Thin Solid Films* **1997**, *304*, 85–97.
(44) Choi, W.; Jung, H.; Koh, S. Chemical shifts and optical properties of tin oxide films grown by a reactive ion assisted deposition. *Journal of Vacuum Science & Technology A* **1996**, *14*, 359–366.
(45) Sanal, K.; Jayaraj, M. Growth and characterization of tin oxide thin films and fabrication of transparent *p*-SnO/*n*-ZnO *p*-*n* hetero junction. *Materials Science and Engineering: B* **2013**, *178*, 816–821.
(46) Kaufman, H. R.; Robinson, R. S.; Seddon, R. I. End-Hall ion source. *Journal of Vacuum Science & Technology A* **1987**, *5*, 2081–2084.
(47) Oudini, N.; Hagelaar, G. J. M.; Boeuf, J.-P.; Garrrigues, L. Physics and modeling of an end-Hall (gridless) ion source. *Journal of Applied Physics* **2011**, *109*, 073310.
(48) Sangaletti, L.; Depero, L. E.; Allieri, B.; Pioselli, F.; Comini, E.; Sberveglieri, G.; Zocchi, M. Oxidation of Sn Thin Films to SnO_2. Micro-Raman Mapping and X-ray Diffraction Studies. *Journal of Materials Research* **1998**, *13*, 2457–2460.
(49) Shanmugasundaram, A.; Basak, P.; Satyanarayana, L.; Manorama, S. V. Hierarchical SnO/SnO_2 nanocomposites: Formation of in situ *p*-*n* junctions and enhanced H_2 sensing. *Sensors and Actuators B: Chemical* **2013**, *185*, 265–273.
(50) Ahn, S.-Y.; Jang, S. C.; Song, A.; Chung, K.-B.; Kim, Y. J.; Kim, H.-S. Performance enhancement of *p*-type SnO semiconductors via SiO_x passivation. *Materials Today Communications* **2021**, *26*, 101747.
(51) Um, J.; Roh, B.-M.; Kim, S.; Kim, S. E. Effect of radio frequency power on the properties of *p*-type SnO deposited *via* sputtering. *Materials Science in Semiconductor Processing* **2013**, *16*, 1679–1683.
(52) Smidt, F. A. Use of ion beam assisted deposition to modify the microstructure and properties of thin films. *International*

Materials Reviews **1990**, *35*, 61–128.
(53) Macleod, H. A. In *Optical Thin Films and Coatings (Second Edition)*, second edition ed.; Piegari, A., Flory, F., Eds.; Woodhead Publishing Series in Electronic and Optical Materials; Woodhead Publishing, 2018; pp 3–23.
(54) Debye, P. P.; Conwell, E. M. Electrical Properties of *N*-Type Germanium. *Phys. Rev.* **1954**, *93*, 693–706.
(55) Hu, Y.; Schlom, D.; Datta, S.; Cho, K. Interlayer Engineering of Band Gap and Hole Mobility in *p*-Type Oxide SnO. *ACS Applied Materials & Interfaces* **0**, *0*, null, PMID: 35609177.
(56) Xu, W.; Li, M.; Chen, X.; Zhao, J.; Tan, R.; Li, R.; Li, J.; Song, W. Synthesis of hierarchical Sn_3O_4 microflowers self-assembled by nanosheets. *Materials Letters* **2014**, *120*, 140–142.
(57) Liang, L. Y.; Liu, Z. M.; Cao, H. T.; Shi, Y. Y.; lian Sun, X.; Yu, Z.; Chen, A. H.; Zhang, H. Z.; Fang, Y. Q. Improvement of Phase Stability and Accurate Determination of Optical Constants of SnO Thin Films by Using Al_2O_3 Capping Layer. *ACS Applied Materials & Interfaces* **2010**, *2*, 1565–1568.
(58) Jiang, Y.-H.; Chiu, I.-C.; Kao, P.-K.; He, J.-C.; Wu, Y.-H.; Yang, Y.-J.; Hsu, C.-C.; Cheng, I.-C.; Chen, J.-Z. Influence of rapid-thermal-annealing temperature on properties of rf-sputtered SnO_x thin films. *Applied Surface Science* **2015**, *327*, 358–363.
(59) Cho, I.-T.; U, M.; Song, S.-H.; Lee, J.-H.; Kwon, H.-I. Effects of air-annealing on the electrical properties of *p*-type tin monoxide thin-film transistors. *Semiconductor Science and Technology* **2014**, *29*, 045001.